

## 3 Experimental Method and Equipment

### 3.1 Method and Principle

The following sections outline the fundamental ideas and perspectives of photoemission from a highly volatile surface, which at first sight would seem incompatible with such a ultra-high vacuum (UHV) electron spectroscopy method. It will be described in detail how a liquid microjet can be constructed, and why the small dimensions together with a suitable streaming velocity allow to measure electron binding energies and electron yields from liquids despite their high vapor pressure. Finally, some basic aspects of photoemission will be presented followed by a short review of the principle properties of synchrotron radiation with emphasize on undulator radiation.

#### 3.1.1 Matching Highly Volatile Surfaces with UHV Electron Spectroscopy

The main obstacle in applying a surface sensitive method, such as electron spectroscopy, to studying processes at liquid interfaces is the principle difficulty to handle a liquid system under vacuum conditions, and to detect photoelectrons originating from the liquid sample. This explains today's still very limited availability of photoemission data from liquids at high pressures in general. The majority of common liquids and solutions are volatile, i.e. they easily evaporate. Therefore, the main problem connected with electron spectroscopy on liquid matter is the vapor pressure, which for typical laboratory solvents may be up to several hundred mbar. This value is substantially higher than the maximum allowable pressure inside an electron energy analyzer. Furthermore, as the liquid surface is covered by dense vapor due to evaporation it is generally impossible to directly assess surface properties by the

experiment. In photoelectron spectroscopy (PES; see section 3.1.3) one has to prevent sample vapor molecules from colliding with the photoelectrons originating from the sample, here the liquid jet, as they are heading for the electron energy analyzer. Note that even if the vapor pressure of a liquid is sufficiently low to avoid collisions in the electron analyzer, the vapor pressure directly above the liquid surface is generally so high that the liquid photoemission spectrum would be entirely masked by that of the vapor. Besides the problem of high vapor pressure of the liquid, which makes it impossible to obtain the required vacuum without either freezing the sample itself or having it consumed by evaporation, one other problem is to maintain a clean surface despite aging processes.

The earliest report on a vacuum surface study of a liquid dates back to an electron diffraction experiment by Wierl in 1930. For grazing incidence he observed electron diffraction rings on a mercury surface which was steadily renewed by overflowing liquid [18]. However, this rudimentary study was not considered particularly successful at that time. Microscopic liquid structure studies by X-ray diffraction were also performed [19], but the results could not be explained satisfactorily. This became possible only later, based on radial distribution functions for intra- and intermolecular pairwise distances [20]. In the early studies of liquid surfaces by means of photoelectron spectroscopy, the liquid was picked up by a rotating target, often a disk (stainless steel [21] or quartz [22]) partially immersed in a liquid reservoir. The rotating wheel drags along a liquid film which can be scraped by a sapphire plate, thus producing a thin liquid layer [23]. In this way a fresh surface of defined liquid layer thickness was obtained and used for molecular beam scattering studies of surface corrugation. In 1981, using monochromatized photons up to 12 eV, the photoelectron threshold energy of liquid water of 10.06 eV was reported for conductor-supported liquids [22]. In another experiment, a liquid film sample was created by a conically shaped metal trundle immersed in the liquid and being rotated about its axis. This arrangement was used for electron spectroscopy for chemical analysis (ESCA) measurements [24, 25] in 1986, however, a large amount of salt had to be added in order to appreciably reduce the vapor pressure [25]. Another variant of generating a liquid film on a substrate surface is the wetted metal wire which serves to continuously transport liquid into the observation region and to minimize the vapor load to the vacuum chamber [24]. In the latter case, the temperature of the liquid was reduced by liquid nitrogen, which lowered the vapor pressure considerably. Generally, previously unaccessible liquids of sufficiently low vapor pressure, ca.  $10^{-2}$  mbar (or respectively low temperature within their liquid range), such as glycol, methanol, toluene, formamide and others, could be investigated. Charging of the low conductive liquid by the electron emission process was

minimized by restricting to very thin films on a metallic substrate. A detailed description of the early liquid surface measurements is given in Ref. [4]. These methods could not be applied to water, though. Similarly, optical absorption measurements in the VUV and XUV spectral range are almost non-existent since again high vacuum is a prerequisite.

Hence, some other experimental technique was required!

### 3.1.2 Liquid Jet: Formation, Theory and Characteristics

One important empirical conclusion of the experiments mentioned above was that the product of the vapor pressure  $p_0$  and the transfer length  $d$  required for transferring photoelectrons to the spectrometer entrance has to be smaller than a characteristic value. For ultraviolet photoelectron spectroscopy (UPS), with photoelectron energies on the order of some tens of eV, the criterion  $p \cdot d < 0.1 \text{ Torr} \cdot \text{mm}$  ( $0.13 \text{ mbar} \cdot \text{mm}$ ) was reported [24]. For volatile liquids, pure water for instance, this requirement can only be fulfilled if a very small surface area of liquid is exposed to the vacuum. One has to imagine a liquid point source, so small, that the number of vapor molecules quickly decreases (for short distances) to a sufficiently low value that both photoelectrons directly emerging from the liquid sample pass the vapor without collisions, and that at larger distance these electrons would reach the electron spectrometer. The solution to that idea was to use a micro-sized liquid jet [26]. This method not only matches high vacuum requirements, but it also provides continuous surface renewal due to the suitably large velocity. Technically, a laminar jet is formed by forcing the liquid through a small pinhole into an evacuated chamber [26]. If the jet diameter is sufficiently small that the Knudsen condition [27] is fulfilled,

$$d_{jet} < \lambda_{mol}, \quad (3.1)$$

a free vacuum surface of a volatile liquid may be achieved. Here,  $d_{jet}$  is the jet diameter and  $\lambda_{mol}$  denotes the mean free path of the molecules at the corresponding thermal equilibrium. From kinetic gas theory  $\lambda_{mol}$  of water molecules at a vapor pressure of 6.13 mbar (4.6 Torr) is estimated to be on the order of  $10 \mu\text{m}$  [26]. The small size of the thin and continuous liquid flow (liquid beam) combined with the low background pressure ( $\sim 10^{-5}$  mbar for water, maintained by heavy pumping) results in nearly collision-free evaporation. Note that the jet indeed guarantees a clean liquid beam surface even in the pressure range of  $10^{-5}$  mbar, because the surface is renewed all the time by its flow. Furthermore the continuous supply of warmer water from the reservoir prevents the beam from freezing as a result of evaporative cooling.

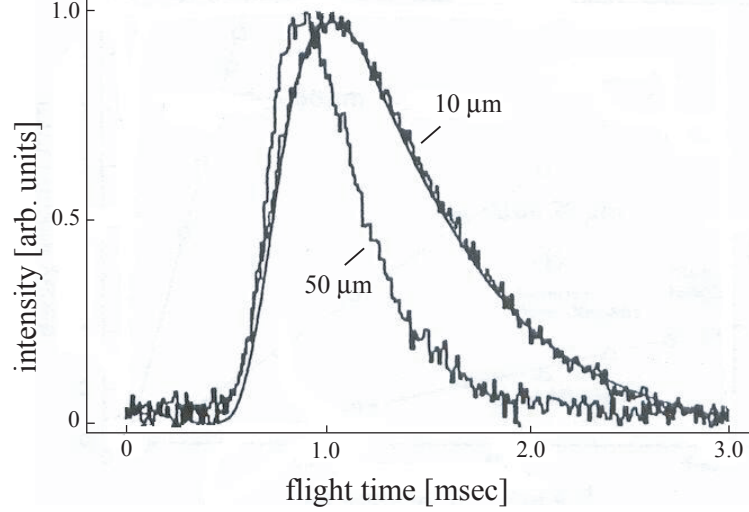


**Figure 3.1:** Time-of-flight spectra of water molecules evaporating from the water jet [28]. For  $10\ \mu\text{m}$  jet diameter a Maxwellian distribution is obtained implying collision-less evaporation. For  $50\ \mu\text{m}$  jet diameter water-water collisions lead to a modified Maxwellian distribution. The former is given by  $f(v) = Av^2 \exp[-m(v-u)^2/k_B T]$ , where a flow velocity  $u$  is superimposed on the thermal velocity distribution;  $v$  is the molecular velocity. Here  $T$  denotes the local surface temperature,  $m$  is the particle's mass,  $k_B$  is the Boltzmann constant, and  $A$  is a fit parameter. The fit in the figure, for the  $10\ \mu\text{m}$  jet, corresponds to  $u = 0$ , and the obtained surface temperature is 281 K.

In order to directly prove collision-free evaporation under the experimental conditions, measurements of the velocity distribution of the evaporated molecules at some distance from the jet had been performed as reported in an earlier work by Faubel [28]. Typical time-of-flight spectra of  $\text{H}_2\text{O}$  molecules are presented in the Fig. 3.1 showing a Maxwellian distribution for a  $10\ \mu\text{m}$  jet, but a narrow supersonic velocity distribution for a  $50\ \mu\text{m}$  jet. The spectra thus confirm the expected transition from the collision to the collision-less regime once the ratio between jet diameter and mean free path approaches the Knudsen limit [28].

Fitting the time-of-flight spectra obtained for the  $10\ \mu\text{m}$  case by a standard Maxwellian velocity distribution function provides a direct measure of the instantaneous local surface temperature of the liquid for the actual vacuum evaporation conditions [28]. In this way a value of 281 K was obtained.

**Jet instabilities and decay.** The thin and continuous water beam is generated by forcing the liquid water (pressurized by 80 bar He) through two sequential (platinum-iridium) pinholes of 200 and  $10\ \mu\text{m}$  diameter into the main vacuum chamber. The ideal, nonviscous flow velocity for a thin wall diaphragm is related to the nozzle backing pressure  $p_0$  and the

liquid density  $\rho$  by the relation:

$$v = \sqrt{\frac{2p_0}{\rho}}, \quad (3.2)$$

obtained by equating  $p_0V$  with the kinetic energy  $mv^2/2$ . For water with  $\rho \simeq 1000 \text{ kg/m}^3$  at  $4^\circ\text{C}$ , the jet velocity is about  $127 \text{ m/s}$ . Directly after the liquid jet emerges from the high pressure behind the nozzle, it forms a straight, laminar flowing, cylindrical filament only within the first 3-5 mm. Very near the nozzle exit, the surface contracts (due to surface tension) within a distance of a few nozzle diameters to its final diameter  $d$  (see Fig. 3.2). For a nozzle with  $10 \mu\text{m}$  diameter a contraction factor of 0.63 was found by laser diffraction measurements of the liquid jet diameter [29]. For larger distances ( $> 3\text{-}5 \text{ mm}$ ) the jet decays into droplets. According to Rayleigh [30], the decay is driven by capillary forces which tend to reduce the energy of a long filament by breaking up the jet into a stream of droplets [4]. Using potential flow theory, it was shown that small spontaneous fluctuations of the jet radius grow exponentially near a critical axial wavelength  $\lambda_c$  and lead to a radial modulation of the jet resulting in its decay into droplets. For practically important cases the wavelength for spontaneous jet decay is [4]:

$$\lambda_c \simeq 4.5d_{jet}, \quad (3.3)$$

and the jet decay length  $L$  is given by the equation [4]

$$L = vt \simeq 3v\sqrt{\frac{\rho d_{jet}^3}{\sigma_{tens}}}, \quad (3.4)$$

where  $\rho$  is the density of the liquid and  $\sigma_{tens}$  the surface tension. Rayleigh theory has been later extended to viscous fluids by Weber [31], in which case the decay wavelength was found to increase as follows

$$\lambda_c = \pi d_{jet} \sqrt{2 + 6K_{Ohn}}. \quad (3.5)$$

Here  $K_{Ohn}$  is known as *Ohnesorge number* which provides an universal scaling number for characterizing jet breakup regions and flow domains [32]:

$$K_{Ohn} = \frac{\eta_d}{\sqrt{\rho \sigma_{tens} d_{jet}}}. \quad (3.6)$$

Here  $\eta_d$  denotes the dynamical viscosity. For values  $K_{Ohn} \ll 1$  the jet flow is non-viscous. Water jets are typical examples for this flow domain.

For a  $6 \mu\text{m}$  water jet (which is the actual jet diameter in the present experiments; see above 3.2.1), assuming  $\rho \simeq 1000 \text{ kg/m}^3$  for the water density,  $\sigma_{tens} = 0.073 \text{ N/m}$  for the surface tension, and a value of  $\eta_d = 1 \text{ mPa}\cdot\text{s}$  for the dynamical viscosity, one obtains  $\lambda_c =$

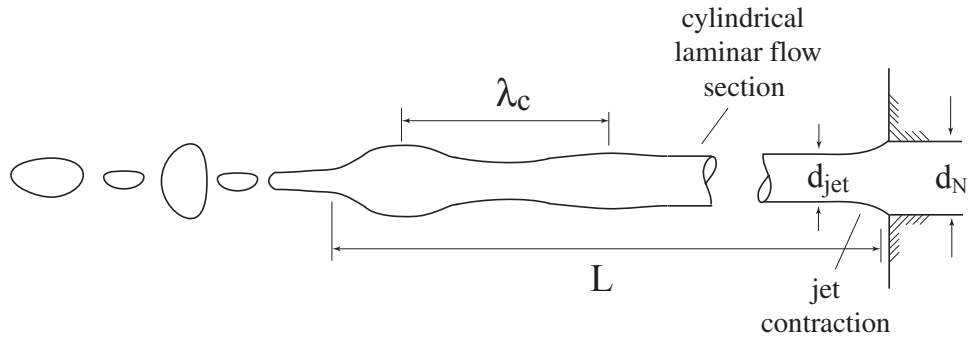


**Figure 3.2:** Schematic of the liquid jet decay into droplets at distance  $L$  from the nozzle. The decay is driven by capillary forces leading to spontaneous amplification of surface waves at a critical wavelength  $\lambda_c$ .

$32\text{ }\mu\text{m}$  using equations 3.5 and 3.6. Then, with equation 3.4 the length  $L$  of the intact laminar jet is calculated to be  $3.5\text{ }\mu\text{m}$ . This is in agreement with laser diffraction measurements from the jet, which were performed at different distances from the  $10\text{ }\mu\text{m}$  nozzle.

Further details as to the role of surface tension and the decay mechanism of a liquid jet, can be found in the pioneering work by Faubel [4].

### 3.1.3 Fundamental Aspects of Photoemission

The electronic structure of matter is one key information for understanding the respective chemical and physical properties. A well established and widely used experimental technique to access this information is photoelectron spectroscopy (PES), a technique based on the photoelectric effect [33]. The subjects of PES are atoms or molecules in the gas phase, solids, and, with special technical requirements, liquids. The outstanding feature of PES is to single out individual electronic states by measuring photoelectron kinetic energies.

One simple approach in describing the photoemission process is the so-called three-step model which considers the photoemission as being *separable* into three distinct and independent processes [35]. At first, the photon is locally absorbed and an electron is excited. In the second step the electron travels through the sample to the surface, and in the last step the electron escapes through the surface into the vacuum where it is detected. This separation is somewhat artificial and, in principle, the whole process of photoexcitation should be treated as a single step.

By absorbing a photon of energy  $h\nu$  a system containing  $N$  electrons and being described by an initial wave function  $\psi_i(N)$  and energy  $E_i(N)$ , will be excited into a final state with

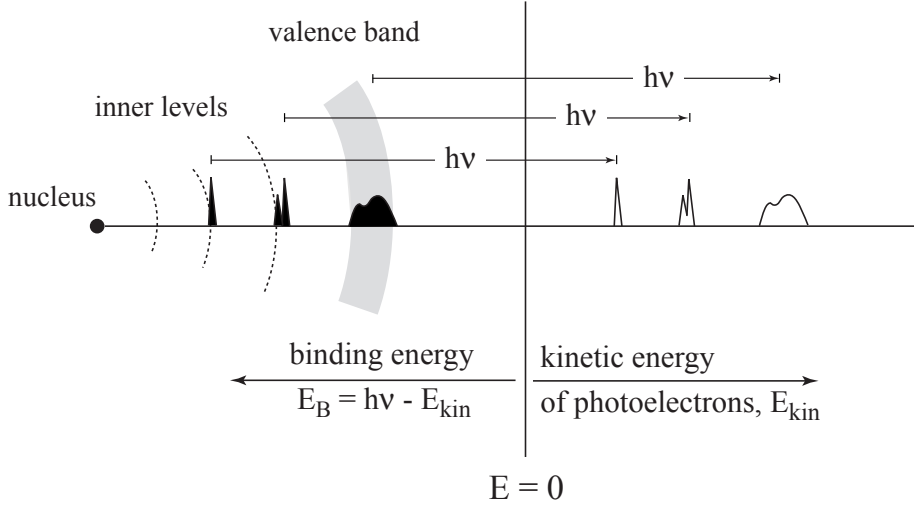


**Figure 3.3:** Illustration of photoelectron spectroscopy [34]. The dashed lines represent the orbitals of the electrons. The binding energy of the photoelectrons is the difference between the energy of the excitation photons and the kinetic energy of the electrons.

$\psi_f(N-1, k)$  and  $E_f(N-1, k)$  and a photoelectron with kinetic energy  $E_{kin}$  will be emitted. Energy conservation gives:

$$E_i(N) + h\nu = E_f(N-1, k) + E_{kin} \quad (3.7)$$

and thus the binding energy relative to the vacuum level may be defined as

$$E_B(k) = E_f(N-1, k) - E_i(N), \quad (3.8)$$

where the final state wave function  $\psi_f(N-1, k)$  represents an atom with a hole in the level  $k$ . If one assumes that no rearrangement of the electrons - either within the atom from which the photoelectron originated or in the neighboring atoms - occurs following the ejection of the photoelectron, then the remaining electrons after an ionization event are described by the same wave function as in the initial state. Within the Hartree-Fock approximation this leads to Koopmans' theorem whereby the ionization energy is obtained directly from the calculation of the neutral ground state [36] and is simply the negative of the atomic orbital energy  $\epsilon_k$  [37]:

$$E_B(k) = -\epsilon_k. \quad (3.9)$$

This approximation is not entirely correct because after ejection of the electron from a particular orbital  $k$ , the system will try to readjust its remaining  $N-1$  charges in such a way as to minimize its energy (relaxation). Therefore, the correct binding energy is given by

the difference between the Koopmans' binding energy  $-\epsilon_k$  and a positive relaxation energy  $E_r$ :

$$E_B(k) = -\epsilon_k - E_r. \quad (3.10)$$

Relaxation is thus a *final state effect*. The assumption that the time needed for the removal of one of the photoelectrons is much shorter than the time required for the rearrangement of the valence electron charge distribution is referred to as the *sudden approximation*.

The time scale for the photoemission event depends on the velocity of the escaping photoelectron and thus the sudden limit corresponds to high excitation energies. It is, however, difficult to formulate strict criteria [38] for the applicability of the sudden approximation, and the energy range within it is valid is still an open question.

At the other limit, known as the *adiabatic excitation limit* the photoelectron leaves the atom slowly, in such a way that the electrons on or near the excited atom will lower their energy by slowly adjusting to the new hole potential in an instantaneous, self-consistent way [39]. This approximation corresponds to low excitation energies.

As previously described, the photoemission process involves the excitation of one electron from an initial state (an atomic orbital) to a final state. The intensity of the photoemission peak (photocurrent) depends on both the initial and final state wavefunctions  $\psi_i, \psi_f$  and of the incident electromagnetic field  $\vec{E}$ . Describing the system's ground state by the Hamiltonian  $H_0$  and the ionizing photon beam as a small perturbation  $H'$ , the transition probability per unit time between the two states is given by Fermi's Golden Rule:

$$w = \frac{2\pi}{\hbar} | \langle \psi_f | H' | \psi_i \rangle |^2 \delta(E_f - E_i - \hbar\omega). \quad (3.11)$$

In the dipole approximation the perturbation can be written as:

$$H' = -\vec{\mu} \cdot \vec{E}, \quad (3.12)$$

where  $\vec{\mu}$  is the dipole moment and  $\vec{E}$  is the external electric field.

PES is an extremely surface sensitive technique due to the strong interaction of the electrons with matter. An electron travelling through a solid will have a certain inelastic mean free path, i.e. a characteristic length that it can travel on the way out of the solid without suffering an energy loss. This length, referred to as electron mean free path, strongly depends on the electron kinetic energy. This relation is known as the *universal mean free path curve* which is shown in Fig. 3.4. The minimum of this curve, in the ca. 20-120 eV range is the region of maximum surface sensitivity (lowest escape depth).



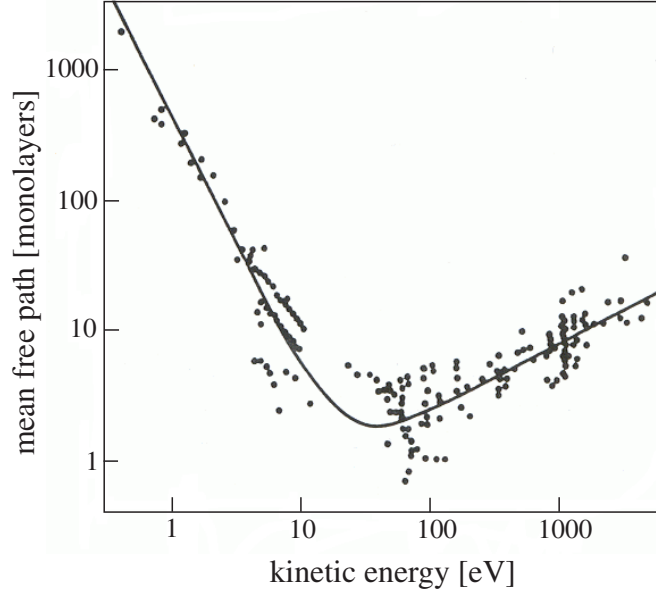


**Figure 3.4:** Mean free path of electrons in solids as a function of their kinetic energy [40].

Since PES requires an incident photon of a known energy value, collimated monochromatic (single frequency) photons are desired. When photons in the ultraviolet (UV) spectral region are used, the technique is called UV Photoelectron Spectroscopy (UPS), with X-ray radiation one refers to XPS or ESCA (Electron Spectroscopy for Chemical Analysis). Using tunable synchrotron radiation one may cover the whole spectral range from the near-UV to the far X-ray regime.

**The angular distribution anisotropy parameter  $\beta$ .** In the dipole approximation the differential cross section  $d\sigma/d\Omega$  for photoionization of a randomly oriented sample by linearly polarized light is defined by [41,42]

$$\frac{d\sigma(h\nu)}{d\Omega}(\Theta) = \frac{\sigma_i(h\nu)}{4\pi} [1 + \beta(h\nu)P_2(\cos\Theta)]. \quad (3.13)$$

Here  $\sigma_i$  is the partial photoionization cross section,  $\beta$  is the asymmetry parameter,  $P_2$  is the 2nd order Legendre-Polynomial ( $P_2(\cos\Theta) = (3\cos^2\Theta - 1)/2$ ), and  $\Theta$  is the angle between the momentum vector of the ejected electron and the polarization vector of the incident photon. The parameter  $\beta$  depends on the photon energy and on the nature of the molecular orbital which is ionized. Possible values for  $\beta$  range between -1 and +2, otherwise the differential cross section in equation 3.13 would become negative.

Knowledge of  $\beta$  is crucial for the proper interpretation of all experimental measurements of photoionization process, unless the measurements are carried out at the *magic angle*,  $\Theta_M$

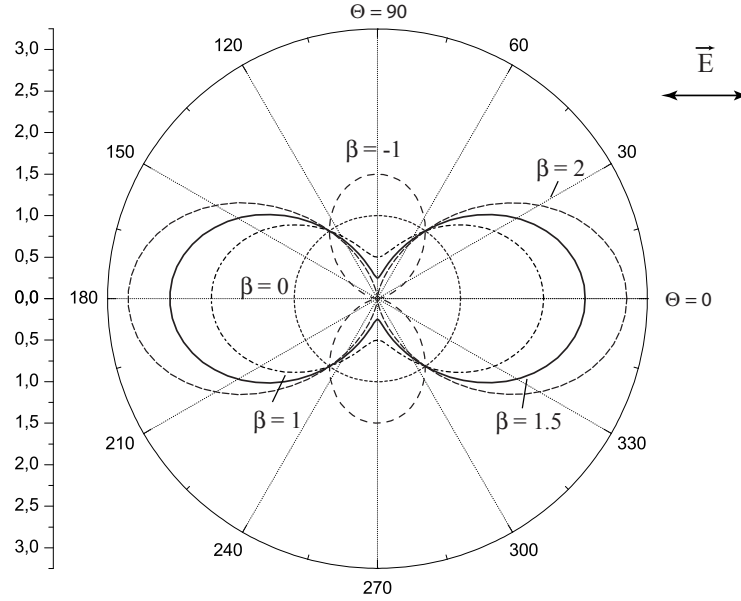


**Figure 3.5:** Angular distribution of photoelectrons for specific values of the anisotropy parameter ( $\beta$ ) and for 100% linearly polarized light. The polarization axis of the light is indicated.

$= 54.7^\circ$  [43], in which case the differential cross section becomes proportional to the total cross section ( $P_2(\cos\Theta_M) = 0$ ).

Fig. 3.5 depicts the angular distribution of the photoelectrons for particular  $\beta$  values, i.e.  $\beta = -1, 1, 1.5, 2$ . The polarization axis of the incoming light is assumed to be horizontal for the figure. For  $\beta = 0$  a fully isotropic distribution is obtained. For  $\beta > 0$  the maximum of the emission is found in the direction of the polarization vector, while for  $\beta < 0$  it is perpendicular to it. From the plot it can be observed that for the *magic angle* the differential cross section is independent of  $\beta$ , i.e. all curves intersect at this angle.

The value of  $\beta$  not only depends on the amplitude but also on the phase shift of the outgoing partial waves and therefore on their interference. Thus, the anisotropy parameter would be expected to be more sensitive to atomic potential changes than the cross section (see section 4.1.3).

### 3.1.4 Synchrotron Radiation and Insertion Devices

Synchrotron radiation is emitted when charged relativistic particles, electrons for instance, are being subjected to centripetal acceleration. In a synchrotron, electrons are accelerated

and confined to nearly circular trajectories by magnetic fields. Due to the relativistic velocities of the circulating electrons, the radiation emission pattern is enhanced into forward direction within a narrow cone, tangentially to the orbit of the electrons. This is explained in terms of a Lorentz transformation of the emission pattern from the particle's coordinate system to the laboratory frame. The natural collimation is one of the important properties of synchrotron radiation. The opening angle of the cone (angular spread) is approximately  $1/\gamma$  [43], with:

$$\gamma = \frac{E}{m_0 c^2}, \quad (3.14)$$

where  $E$  is the energy,  $m_0$  the mass of circulating electrons and  $c$  the velocity of light ( $\gamma = 1/\sqrt{1 - (v/c)^2}$  is the electron's Lorentz factor;  $v$  is the velocity of electrons). The higher the kinetic energy of the charged particles the narrower the emission cone becomes, and the spectrum of the emitted radiation extends to higher energies.

Due to its properties synchrotron radiation is by far superior to conventional light sources such as X-ray tubes or discharge lamps. Synchrotron radiation not only allows for a wide energy range (from IR to hard X-ray), but also for high flux, small spot size and a high degree of polarization. Yet, other techniques, such as laser plasmas or high harmonic generation from gas jets, for instance, may be advantageous for some applications.

Typically, the spectral intensity of synchrotron radiation is characterized by its brilliance [43] which is defined as:

$$B = \frac{(\text{spectral flux into } 0.1 \% \text{ bandwidth})}{\text{source area } (mm^2) \cdot \text{solid angle } (mrad^2) \cdot 100(mA)}. \quad (3.15)$$

Brilliance is thus proportional to the number of photons normalized by the source area, horizontal and vertical divergences at 100 mA ring current.

Generation of synchrotron radiation requires the coordination of several systems: (i) the electron production stage, (ii) a primary accelerating system for the electron beam, and (iii) a storage ring to store the electrons for several hours. Finally, one needs (iv) outlet (front-end) systems to guide the photon beam to the experiment. This is achieved with vacuum tubes (beamlines) either following a bending magnet or an insertion device (IDs, see below). Optical elements direct the light to a monochromator, which selects the desired photon energy.

As the experiments presented were performed at the electron storage ring BESSY II in Berlin, some features of this facility will be described below. Electrons emitted by a cathode are accelerated to an energy of 100 keV. The second stage is a microtron, the central part

of which is a linear accelerator with a strong high frequency electrical field (3 GHz). As a consequence, the circulating electrons are bunched and they will achieve at this point an energy of 50 MeV. From the microtron electrons are transferred into the vacuum chamber of the synchrotron (booster) where they are further accelerated to a final energy of 1.7 GeV. As the electron energy increase would lead to a larger trajectory, magnetic field corrections are necessary to keep the particles on the same orbit. From this synchronization of field and energy, the name *synchrotron* evolved. Finally, the electrons are injected through a transfer channel into the storage ring.

The **storage ring** is an accelerator designed to keep the electrons in a closed orbit at relativistic but constant velocity. BESSY's storage ring has a circumference of 240 m containing 16 straight sections. Each straight section is followed by bending magnets deflecting the electron beam into the next section. The circulating electrons have transverse motions with respect to the ideal path, which cannot be compensated for by the dipole magnets only. Hence, in order to keep the electrons within the closed orbit, additional focusing magnets, such as magnetic quadrupoles and sextupoles, for focusing in horizontal and vertical plane, respectively, are required.

The electrons circulating in the storage ring constitute an electric current, with a maximum value of 0.3 A (roughly  $2 \times 10^{12}$  circulating electrons) at BESSY; this value is typically achieved directly after injection. With a lifetime of 5-10 hours the current drops to about half of its value at which point the ring will be refilled. These current losses arise from electron-electron collisions (Touschek effect), and from electrons scattered by residual gas molecules ( $10^{-10}$  mbar base pressure in the ring).

Energy losses due to the emission of synchrotron radiation are compensated by four cavity resonators operated at 500 MHz, which re-accelerate the electrons (back) to their nominal energy of 1.7 GeV. The radio frequency (RF) determines the interbunch spacing, which is 2 ns in multi-bunch mode (MB). In the storage ring, recoupling of the positive ions with the electron beam causes distortion of life time and beam quality. By means of a dark gap in the fill pattern these ions can be shaken off. Thus, in MB mode only 320 bunches are filled out of 400 possible. Yet, other modes may be run, single-bunch (SB) and hybrid bunch (HB), respectively. The former corresponds to one single bunch in the ring and its repetition rate is determined by the round trip time. In the case of the BESSY storage ring (240 m circumference), the time for one revolution is 800 ns (1.25 MHz). For typical ring currents the BESSY synchrotron pulse width is about 30 ps in MB mode and 60 ps in SB mode. The smaller width in MB results from the lower number of electrons in each bunch, which in turn

leads to a weaker electrostatic repulsion within each bunch and therefore to shorter bunches. For further details as to the temporal structure of the SR pulses, see Appendix 6.2.

**Insertion devices**, i.e. undulators and wigglers, are magnetic arrays located within straight sections of the storage ring. The magnets are arranged periodically. Such an array of  $N$  periods (with period length  $\lambda_0$ ), forces the electrons to move on a periodically wiggled trajectory over the length of the device (see Fig. 3.6). At each curve radiation is being emitted in the forward direction, the individual intensities generated at each curve add up (either additive or coherently, see below), and the total light intensity increases with the number of poles in the electron path. Undulators and wigglers differ by their magnetic field value. Specifically, wigglers produce higher magnetic fields but have fewer magnetic poles than undulators. A characteristic parameter  $K$  for these devices relates the maximum deflection angle of the electron path  $\alpha$  to the natural opening angle  $1/\gamma$  [43] of the emitted radiation and is given by:

$$K = \frac{\alpha}{1/\gamma} \simeq 0.934 B_0 \lambda_0, \quad (3.16)$$

where  $B_0$  is the amplitude of the magnetic field (in Tesla) and  $\lambda_0$  is the period length of the magnetic array (in cm).

Depending on the  $K$ -value, the cones from individual wiggles either contribute *separately*, as the sum of individual intensities ( $K \gg 1$ , the device is called a wiggler), or they add *coherently* ( $K \leq 1$ , the device is called an undulator).

For  $K \gg 1$ , the deflection is larger than the angular width of the emission. In this case the cones from the individual wiggles contribute non-coherently to the intensity in the horizontal plane and produce an intensity gain which is  $2N$  times the value of the corresponding radiation from the deflection in a single wiggle.

For  $K \simeq 1$ , the insertion device is called an undulator and the major difference with respect to the wiggler is that constructive interference occurs more strongly in the former case (the light cones from the individual wiggles overlap causing interference effects between electromagnetic waves emitted from the same electron at different positions on its travel through the magnetic field). This causes the spectral intensity to be concentrated on certain wavelength ( $\lambda_n$ ). As a result quasi-monochromatic light [43] of high brightness is being obtained:

$$\lambda_n = \frac{\lambda_0}{2\gamma^2} \frac{1}{n} \left( 1 + \frac{K^2}{2} + \gamma^2 \theta^2 \right) \quad n = 1, 2, 3 \dots \quad (3.17)$$

Here  $\theta$  denotes the emission angle with respect to the undulator axis and  $n$  is the number of the harmonic (for  $n = 1$  the fundamental radiation is obtained). The energy width of the

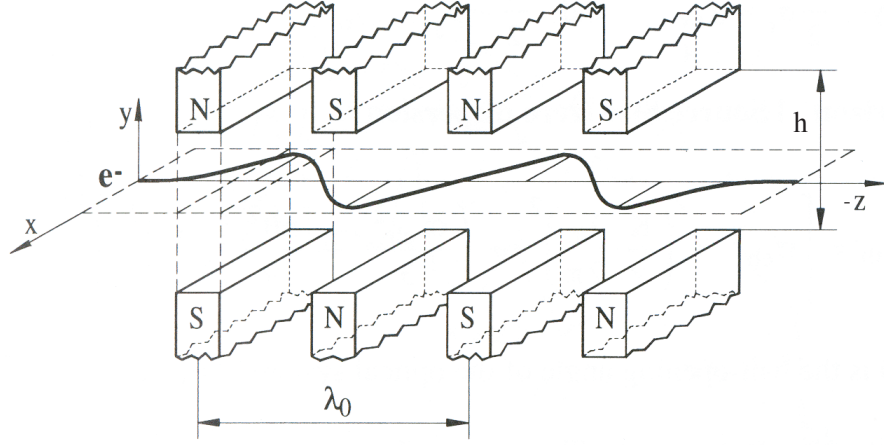


**Figure 3.6:** Schematic of the magnet structure of a wiggler/undulator and of the electrons' trajectory [44]. The magnets gap is designated here by  $h$ .

harmonics depends on the number of undulator periods  $N$ , and is given by  $\Delta E = E/N$ . As an example, this yields a value of  $\Delta E \simeq 2 \text{ eV}$  for the present undulator U125 ( $N = 32$ ), for 60 eV first harmonic.

For  $K \ll 1$ , the spectrum is mainly composed of a single strong peak at the fundamental frequency  $\nu_1$ ; for larger  $K$ , the relative intensity of the higher harmonics is increased.

From equation 3.17 the wavelength ( $\lambda$ ) and photon energy of the emitted radiation ( $\epsilon$ ) may be expressed in practical units ( $\lambda [\text{\AA}]$ ;  $\epsilon, E [\text{eV}]$ ) [45] as following:

$$\lambda = 1305.6 \frac{\lambda_0}{E^2} \frac{1}{n} \left( 1 + \frac{K^2}{2} + \gamma^2 \theta^2 \right), \quad (3.18)$$

$$\epsilon = 9.498 n \frac{E^2}{\lambda_0 \left( 1 + \frac{K^2}{2} + \gamma^2 \theta^2 \right)}. \quad (3.19)$$

Notice that the fundamental wavelength of the radiation is shorter than the period of the undulator because of the large  $\gamma^2$  term ( $\gamma = 1954 \cdot E [\text{eV}]$ ). The wavelength of the radiation can be varied either by changing the electron beam energy ( $\gamma$ ) or the insertion device magnetic field strength, and hence the  $K$  value (equation 3.16). The magnetic field can be easily varied by changing the distance between the magnets ( $h$ ; see Fig. 3.6), i.e. by changing the undulator gap. This is what was actually been done for each photon energy variation in the experiment.

Undulator radiation possesses a degree of polarization higher than 98 %. For a planar undulator the light has linear polarization, the direction of which is in the plane of oscillation

of the electron trajectory, i.e. in the plane of the floor. By arranging the poles in specific geometries it is possible to produce circularly or elliptically polarized light (e.g. APPLE type undulators).

## 3.2 Setup and Equipment

The following section describes in detail the entire experimental setup used for the present measurements. This includes the jet apparatus, the working principle of the electron spectrometer and the MBI undulator beamline.

### 3.2.1 Liquid Jet Apparatus

The water-jet experiment constitutes one out of two end stations of the MBI beamline at BESSY II. The other is a surface experiment devoted to two-color two-photon photoemission (2C-2PPE; see section 6.2) solid-surface experiments. The jet apparatus consists of four major vacuum chambers: the cubic interaction chamber (I), the cryo-pumped chamber (II), differential pumping stage (III), and the spectrometer chamber (IV), see Fig. 3.7.

As already mentioned (page 19), the jet is formed by injecting the liquid water at 4 °C temperature (backed at 80 bar helium pressure) through a small aperture into the vacuum chamber. The straight beam passes in front of the 100  $\mu\text{m}$  entrance of the electron spectrometer (in the cubic chamber (I), see Fig. 3.10 ) at ca. 1 mm distance (fulfilling the transfer length condition  $p \cdot d < 0.13 \text{ mbar} \cdot \text{mm}$  [26], see also 3.1.2), and condenses on a  $\text{LN}_2$  cold trap after travelling about 60 cm distance through the cryo-pumped chamber, see Fig. 3.7.

A valve separates the spectrometer chamber from the main chamber, which is necessary for two reasons. First, the cubic interaction chamber (I) is being frequently vented to atmospheric pressure during experimental periods. This is, for instance, required when cleaning the skimmer or for removing the accumulated salt layers from the inner walls, which is typically necessary prior to starting a new experimental run. Secondly, the liquid jet needs to be *started* at atmospheric pressure (see below), otherwise the water in the nozzle channel would freeze by evaporative cooling and thereby damage the opening due to expansion of water at freezing. The small orifice (100  $\mu\text{m}$ ) in front of the spectrometer, the skimmer, serves as a differential pumping stage between the electron spectrometer chamber and the cubic interaction chamber. This yields a base pressure of  $10^{-8}$  mbar in the former chamber, as compared with the  $10^{-5}$  mbar pressure determined by the water jet, in the latter chamber.

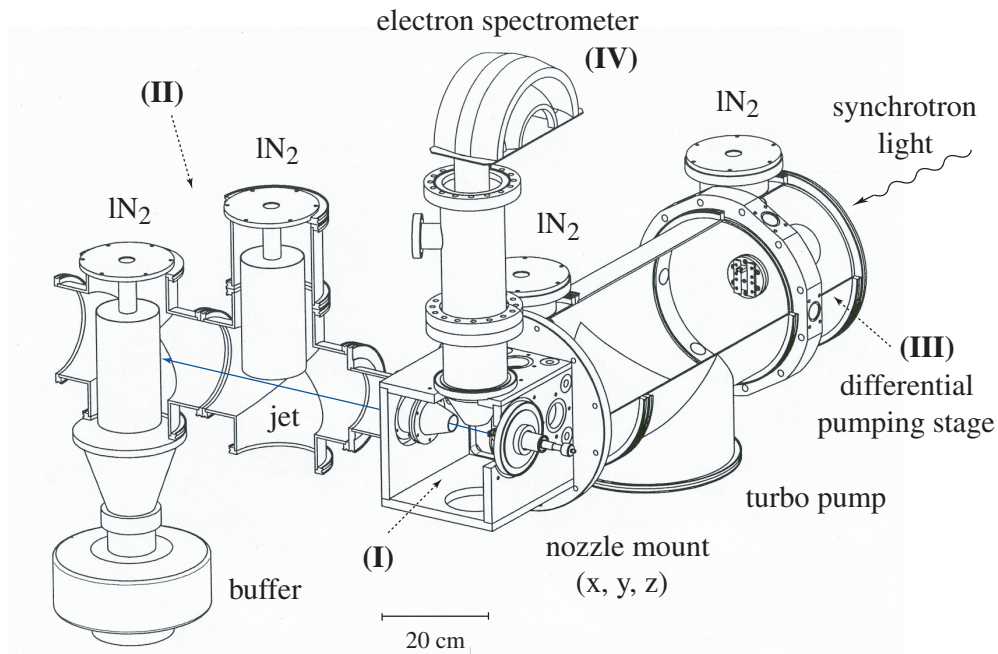


**Figure 3.7:** Schematic of the water jet apparatus at BESSY II. (I) main interaction chamber, (II) cryo-pumped chamber, (III) differential pumping stage, (IV) spectrometer chamber. The synchrotron light intersects the water jet perpendicularly (as indicated).

The  $10^{-5}$  mbar working pressure is maintained using a 1500 l/s turbo pump in conjunction with  $\text{LN}_2$  cold traps. Another differential pumping stage (III) allows the coupling to the vacuum system of the beamline ( $10^{-9}$  mbar) within 30 cm distance. This unit was specially designed to make the liquid photoemission experiment possible at MBI-BESSY beamline.

The water droplets are cooled so quickly that they become frozen ice filaments upon reaching the  $\text{LN}_2$  cold traps (II)<sup>1</sup>. The amount, size and structure of these filaments, or *ice needles*, vary from salt to salt. Some may have a length of about 10 cm, or longer, before breaking. An experimental running time can last many hours, resulting in a considerable pile of ice needles within the cryo-pumped (II) chamber. This leads to the concern that the ice needles could extend the full chamber length and proceed to hit the nozzle mount. An U-shaped ice cutter was installed into the apparatus at a midway point between the cold traps and the nozzle mount to provide manual control over the ice needles' growth. Fig. 3.8

<sup>1</sup>The jet is in fact supercooled. This metastable state undergoes a phase transition (from liquid to crystalline structure) on a time scale larger than the arrival time at the  $\text{LN}_2$  traps. Hence the traps 'catch' the beam rather than freezing it.



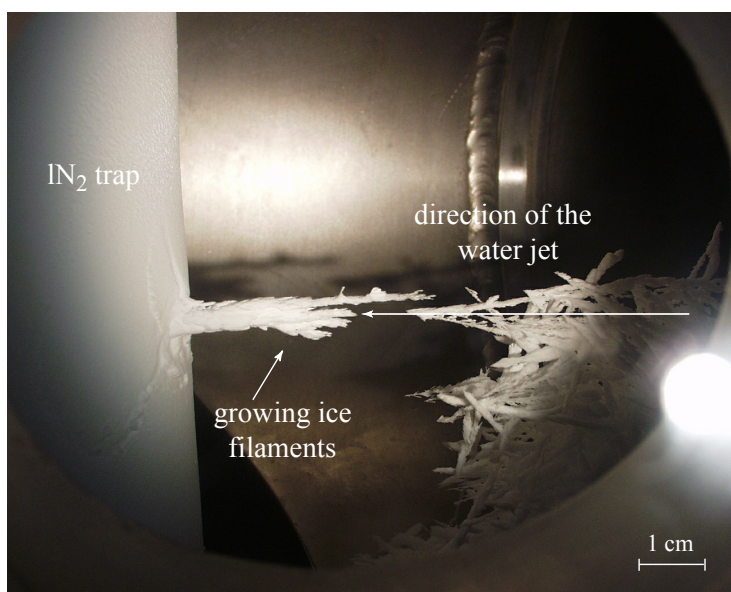


**Figure 3.8:** Ice filaments from 3M NaI aqueous solution growing at the LN<sub>2</sub> cold trap.

shows a typical photograph of the ice filaments growing at the LN<sub>2</sub> cold trap.

A new problem arises when conducting experiments on alcohols, which do not freeze into ice needles, but rather transform into a highly viscous liquid film. These films slowly flow down the cold-trap wall and increase the residual chamber pressure. To avoid this, a LN<sub>2</sub> buffer can be optionally mounted at the bottom of the chamber which freezes the cold liquid dripping down.

Optimum alignment of the water jet is possible by adjusting both the nozzle, mounted on a xyz-manipulator (precision  $< 5 \mu\text{m}$ ), and the entire chamber (XYZ) by its mounting frame. A screen ( $1 \times 1 \text{ cm}^2$ ), covered by fluorescent material, was mounted inside the chamber and can be inserted into the synchrotron-light path to reveal, via the observed fluorescence, the approximate location of the synchrotron beam. A CCD camera fixed at the bottom of the chamber transmits an enlarged image of the interaction region to a TV screen, which facilitates accurate alignment of the water jet and the synchrotron beam directly below the  $100 \mu\text{m}$  aperture of the skimmer.

In the main chamber (I) the synchrotron light intersects the liquid jet perpendicular to its propagation direction just at the point of the spectrometer entrance. The electron detection axis is perpendicular to both the jet propagation and the light path as shown by photograph in Fig. 3.9 and also schematically in Fig. 3.10. Note that for the present

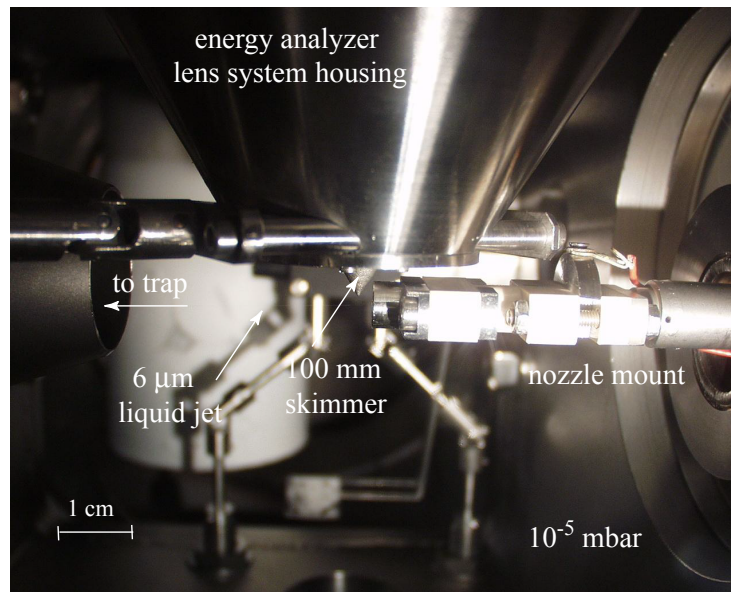


**Figure 3.9:** View inside the interaction chamber (I). The jet propagates from right to left, and the synchrotron light arrives perpendicular to the paper plane.

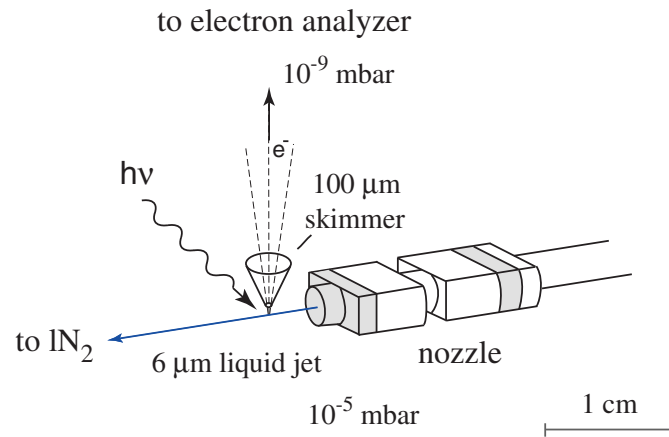


**Figure 3.10:** Schematic detailing the directions of the water jet, the synchrotron light and the photoelectron detection (compare Fig. 3.9). The light polarization vector is perpendicular to the photoelectron detection.

experiments the synchrotron light polarization vector is parallel to the jet direction while electrons are detected perpendicular to the light polarization vector.

With a spectrometer entrance of  $100\ \mu\text{m}$  diameter, in a distance of 1 mm from the liquid jet, photoelectrons are detected in an angular range within  $\pm 3$  degrees in a direction normal

to the liquid-jet axis. The photoelectron detector is a hemispherical electron energy analyzer (Specs/Leybold EA10/100) with water compatible stainless steel electrodes and a secondary electron multiplier (SEM). For 10 eV pass energy, as has been used throughout the experiments, the energy resolution is about 20 meV. The *overall* experimental resolution in the present case is, however, considerably lower, about 200 meV, attributed to our choice of a rather low synchrotron photon energy resolution (large exit slit). This was necessary in order to obtain reasonably high photoemission signal from this very small target. Notice that the photoemission peaks from the liquid water are much wider, ca. 1 eV. The housing chamber was modified to accommodate two differential pumping stages (both 240 l/s turbomolecular pumps), one for the electron optics region and the other for the hemisphere section. In order to prevent work function changes due to condensation of water within the spectrometer, this chamber (IV) was permanently kept at ca. 100 °C. The spectrometer is mounted on top of the main chamber with its axis normal to the floor, see Figs. 3.7, 3.9, and 3.10.

A Helmholtz cage ( $1.20 \times 1.20 \times 1.20 \text{ m}^3$ ) surrounds the whole apparatus in order to compensate for the deflection of electrons by the Earth's magnetic field. Prior to each measurement the magnetic field inside the chamber is validated with a Gaussmeter and then compensated for using the coils.

**Water Tanks and Nozzle Mount.** Two identical 400 ml cylindrical reservoirs (Fig. 3.11) are used for storing and dispensing, of both the water and the solutions, during the measurement. This twin water-pipe system, fully connected through a series of valves, allows for the possibility of continuous measurement for 10 hours without breaking the vacuum. Our standard procedure requires frequent control measurements on pure water, thus one of the tanks is only used for pure water and the other one contains the salt solutions. For the present experiment highly demineralized water was used.

Switching between salt solutions can be accomplished within about 1 hour. The solution tank is first flushed with water several times before being filled with the desired solution. For further confirmation of the full removal of all previously accrued salt particles from the inner tanks' walls, the solution pipe is first filled with pure water and the jet is run until the photoemission spectrum of pure water is obtained. To introduce the new solution into the system, a membrane pump (chemicals resistive) is used to create vacuum, which in turn draws the liquid up into the pipes. In order to force the liquid from the reservoirs through the capillaries and the nozzle, 80 bar He pressure is applied to one end of the tanks; see Fig. 3.11.

The liquid passes through a filter (porous steel;  $0.2 \mu\text{m}$  pore diameter) on its way to the

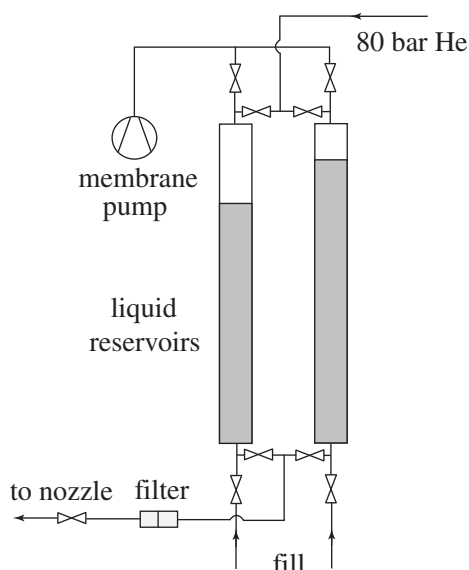


**Figure 3.11:** Schematic of the water reservoirs. The tanks are pressurized by 80 bar He in order to achieve the required flow velocity.

nozzle. The injection system and the nozzle support are displayed schematically in Fig. 3.12. The jet is formed by forcing the liquid through two sequential (platinum-iridium) pinholes (nozzles) of 200 and 10  $\mu\text{m}$  diameter, respectively. This latter nozzle is often damaged due to salt residue from the passing solution. The 10  $\mu\text{m}$  diameter nozzle has to be submerged in water when mounted, as it is imperative to have no air in the system. A small water bubble is formed at the end of the nozzle mount, the nozzle plate is inserted into the water bubble at an angle, and then fixed into its appropriate depression. Although this nozzle is 10  $\mu\text{m}$  in diameter, the innate surface tension properties of water force the jet to contract to about 6  $\mu\text{m}$ ; for more details see section 3.1.2. The 200  $\mu\text{m}$  nozzle was found to be useful in stabilizing the electrochemical potential in the vicinity of the final 10  $\mu\text{m}$  exit nozzle; it thus serves as a kind of a *guard electrode*. Both metal nozzles are electrically grounded in order to rule out charging upon photoemission. Principally, electrokinetic effects may lead to an additional surface streaming potential arising from the transport of charge by the flowing jet. This is associated with surface charge separation of the Helmholtz layer at the liquid-metal interface [46]. However, as pointed out earlier [26, 28, 47], charging of the insulated surface is negligible for a flowing micro-sized system.

The jet is introduced into the chamber at atmospheric pressure to avoid damaging the nozzle by freezing. Once the jet runs, the pumping of the main chamber can be started, and

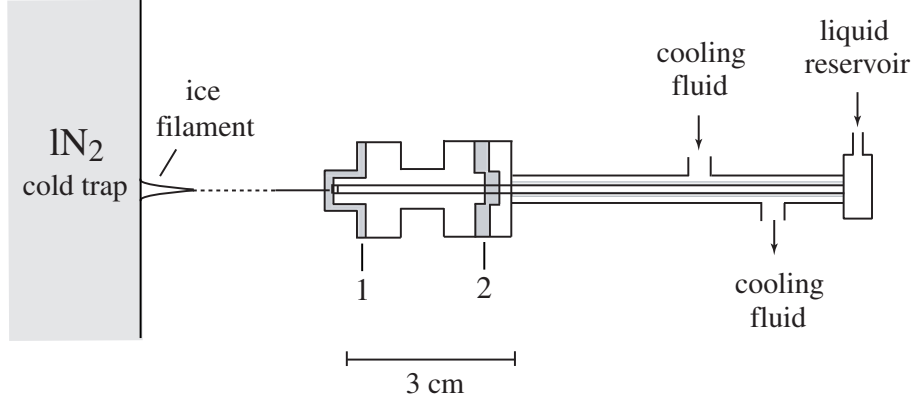


**Figure 3.12:** Injection system and nozzle support. 1 and 2 denote the mounts for  $10\mu\text{m}$  and  $200\mu\text{m}$  nozzles, respectively.

stable measuring conditions are achieved in within less than 1 hour.

### 3.2.2 Electron Spectrometer

A schematic of the spectrometer and the electronics is shown in the Fig. 3.13.

The hemispherical analyzer consists of two hemispheres having the same center point but different radii. The resulting mean radius  $R_0$  is 100 mm. A potential difference  $\Delta V$  is applied between the surfaces so that the outer hemisphere is negative and the inner one positive with respect to  $\Delta V \times R_0$ , which is the median equi-potential surface between the hemispheres. The photo-electrons ejected from the jet pass through the first electrostatic lens element that focuses them on the analyzer entrance and *adjusts* their energy (accelerates or de-accelerates depending on their initial kinetic energy) to match the pass energy of the analyzer. The analyzer is a band pass filter only transmitting electrons with an energy very near to the pass energy  $E_{pass}$ , which are then detected at the channeltron detector. The pass energy is given by

$$E_{pass} = (-q)k\Delta V, \quad (3.20)$$

where  $\Delta V = V_{ext} - V_{int}$ , is the potential difference applied between the two hemispheres, and  $k$  is a spectrometer calibration constant with a value of 1.383 for the analyzer used in the present experiment. Entering the hemispheres, the photoelectrons will experience a centripetal force and hence undergo uniform circular motion. The curvature radius of this motion for a given potential difference between the hemispheres is determined by the electron's velocity, which is directly related to the electron's kinetic energy. Electrons having

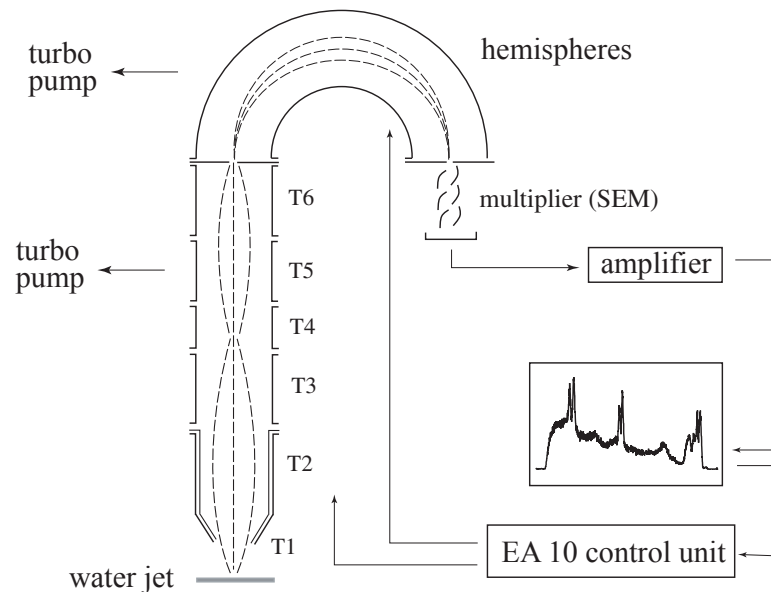


**Figure 3.13:** The path of the electrons inside the hemispherical electron analyzer and schematic of the electronics.  $T_i$  denote electrostatic lenses.

an energy equal to the pass energy follow the central trajectory, whereas the ones having higher or lower energies will be deflected less and more, respectively. By varying the potential difference between the two hemispheres of the spectrometer, a kinetic energy spectrum of the photoelectrons for a given incident photon energy can be reconstructed.

The kinetic energy of the electrons can be typically scanned in two different operating modes:

- by varying the retardation ratio while holding the analyzer pass energy constant (Fixed Analyzer Transmission FAT)
- by varying the pass energy while holding the retardation ratio constant (Fixed Retarding Ratio FRR)

The data presented here were taken in the FAT mode. In this mode the resolution is constant throughout the whole kinetic energy range.

The analyzer has a finite energy resolution  $\Delta E$  which is dependent on the chosen mode of operation and specific operating conditions. The energy resolution is given approximately by

$$\Delta E = E_{pass} \cdot \left( \frac{d}{2R_0} + \alpha^2 \right), \quad (3.21)$$

where  $d$  is the slit width,  $R_0$  the mean radius of the hemispheres and  $\alpha$  half angle of the electrons entering the analyzer (at the entrance slit). For the EA 10/100 and a typical pass energy of 10 eV,  $\Delta E$  is about 20 meV.

Inside the tube and analyzer chamber,  $\mu$  metal shielding is used to minimize the influence of external magnetic fields which could deflect the electrons.

### 3.2.3 MBI Undulator Beamline at BESSY II

Usually, the radiation from the insertion device, even though it is considerably monochromatic (see section 3.1.4) is still not suited for PES. A distribution of photon energies would complicate the electron spectra, broaden the structures and hinder selective resonance excitations. Hence, further monochromatization is required.

The high-resolution electron energy analyzers have source sizes in the order of few tenths of millimeter or even lower. For obtaining maximum signal, the size of the synchrotron beam should be the same or even smaller than the source area. In order to focus and to transfer the light from the front-ends to the experimental end stations it is necessary to direct it by optical elements through monochromators.

Monochromators used in the VUV region of the synchrotron radiation use reflective gratings to select a certain band pass of wavelengths out of the emitted spectrum. This is based on the grating equation

$$\sin \theta_i + \sin \theta_d = m\lambda N, \quad (3.22)$$

where  $\theta_i$  and  $\theta_d$  are the incidence and diffraction angles and  $m$  is an integer number that specifies the diffraction order. The number of lines per millimeter on the grating is given by  $N$ . Depending on the wavelength, the light is diffracted under different angles and thus it is possible to select the desired energy that passes the monochromator. An important parameter describing the relative energy width  $\Delta E$  around the center value  $E$  is the resolving power  $R = E/\Delta E$ .

The beamlines have to be maintained under ultra-high vacuum (UHV) conditions because otherwise the ultraviolet (UV) and soft X-ray radiation would be absorbed by gaseous molecules. In addition, vacuum conditions largely prevent the mirror and grating surfaces from contamination.

The experiments described here have been performed at the Max-Born-Institut facility at the BESSY II storage ring, Berlin. This user facility is dedicated to combined laser-synchrotron two-color two-photon photoemission (2C-2PPE) experiments. Typically, the

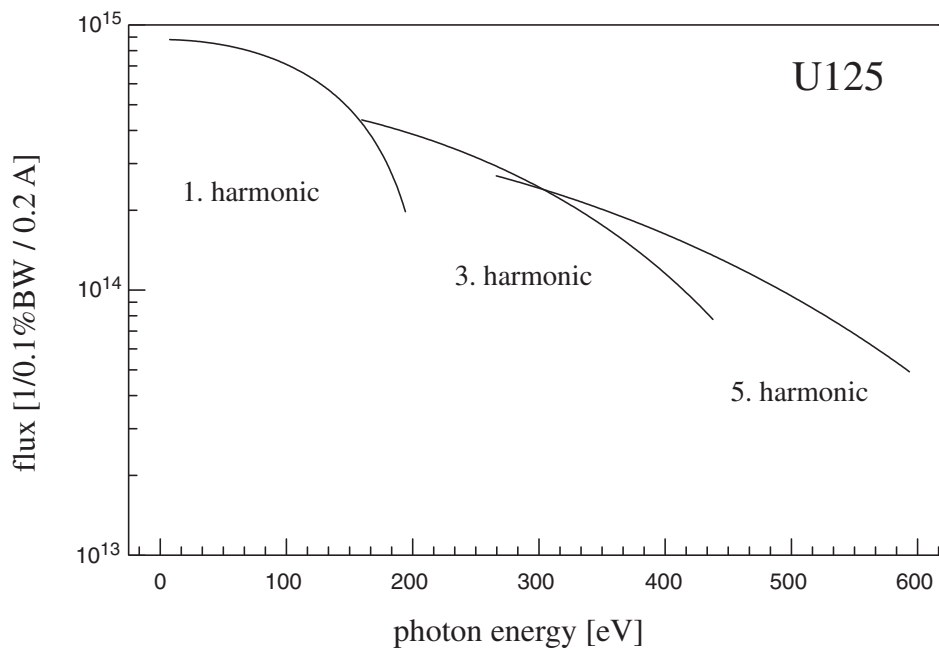


**Figure 3.14:** Photon flux of undulator U125/1 for 0.2 A ring current.

laser provides the pump pulse and the synchrotron the probe pulse, the latter suitably time-delayed. The XUV source for this beamline is an undulator (U125) with a periodic length of 125 mm. Photon fluxes of the U125 obtained for 0.2 A ring current are presented in Fig. 3.14. The MBI monochromator operates in the photon energy range 20 to 180 eV with a resolving power better than  $10^4$ . For the present water-jet experiment lower resolution was used in order to increase the photoemission signal.

The light from the U125 undulator is deflected by a toroidal mirror into the beamline and focused on the entrance slit of the grazing incidence monochromator with an object to image ratio of 10:1. The spherical grating focuses the radiation on the exit slit of the monochromator. Apertures before and after the grating chamber limit the beam profile. The final focal size is achieved by two toroidal refocusing mirrors which direct the synchrotron radiation into either one of the two end stations, an UHV surface apparatus and a water microjet apparatus. The overall length of the beamline, from the front-end to the experiment, is approximately 20 m, including the monochromator of about 10 m length. A schematic drawing of the beamline is shown in Fig. 3.15.

The construction of the beamline and the monochromator was based on extensive ray-



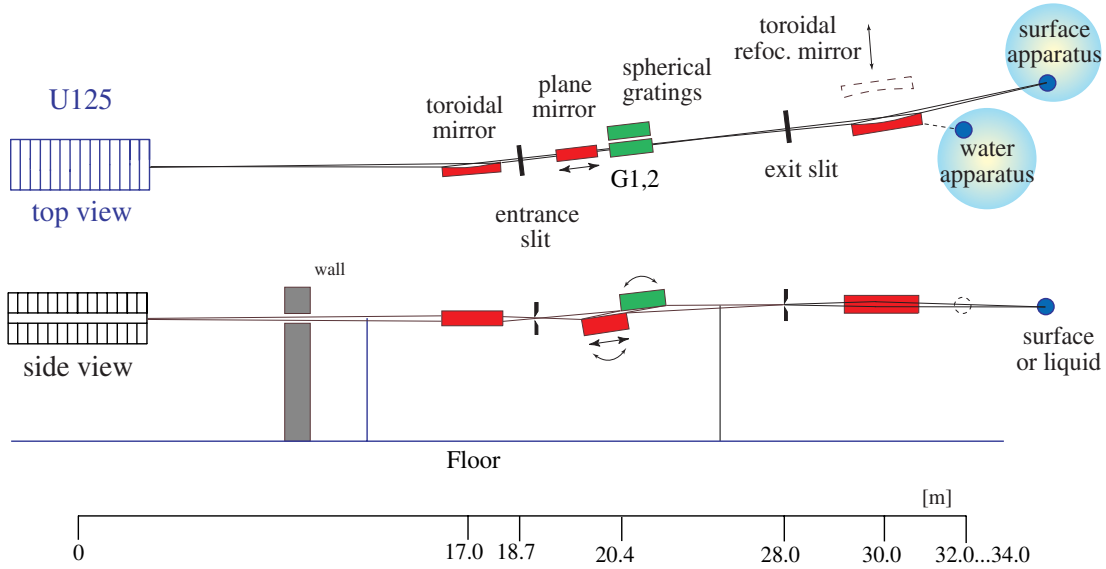


**Figure 3.15:** Schematic of the MBI-Beamline at BESSY II at the U125/1 undulator (top and side view). The main components of the monochromator are a plane mirror and two spherical gratings,  $G_1$ ,  $G_2$ , covering the 30-140 eV photon energy range. Two interchangeable toroidal refocusing mirrors allow to direct the synchrotron light to either the water apparatus or to a surface experiment.

tracing calculations which have been carried out with state-of-the-art programs supplied by BESSY GmbH. Based on these calculations a spherical grating monochromator (SGM) was chosen. The monochromator design is illustrated schematically in Fig. 3.16.

In order to cover the specified energy range, two interchangeable toroidal gold-coated gratings (700 lines/mm, 1666 lines/mm) are used, which can be moved into the optical path (under vacuum conditions). The monochromator is based on the VIA-principle (variable included angle) - a plane mirror (PM) can be translated and simultaneously rotated so, that the central ray always hits the center of the spherical grating (SG) which can also be rotated about its center. The advantage of this scheme is that the deflection angle  $2\Theta$  is a free parameter that can be used to fix the position of the slits during a scan. The path lengths in the monochromator are thus kept almost constant over the whole energy range. In order to achieve the spectral resolution specified above, the precision of the plane mirror positions

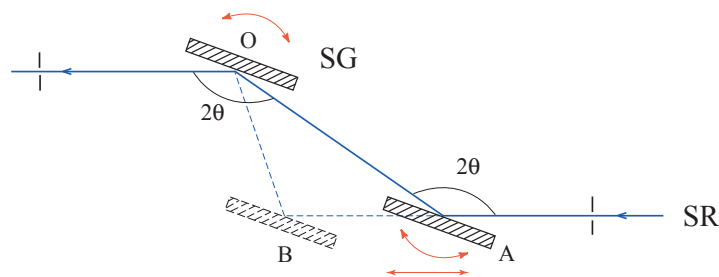


**Figure 3.16:** Principle of the MBI spherical grating monochromator at BESSY II (undulator U125). A and B are the two extreme positions of the plane, rotatable gold-coated mirror. O is the center of the spherical grating and  $2\theta$  is the deflection angle of the synchrotron light.

must be in the order of  $0.5\mu\text{m}$  and the angles have to be set with a resolution better than  $0.2\text{ arcsec}$ . These requirements are fulfilled with computer controlled stepper gear boxes and micrometer screws. Additionally, a 2-axes laser interferometer is inserted to control the plane mirror position and correct it with piezo actuators.

To change the transmitted wavelength, the grating and the mirror inside the monochromator have to be rotated and positioned according to precalculated trajectories, which were determined by the ray tracing calculations. Synchronized with these movements the undulator gap has to be adjusted as well. In order to coordinate this complex technique, BESSY has developed specific standards for the control system, and offers specific tools based on the internal CAN-bus and on VME-bus systems linked to the experimental units by IEEE and RS232 interfaces.

With a 1:1 imaging of the monochromator exit slit, a spot size at the sample position of about  $250\mu\text{m} \times 120\mu\text{m}$  for the water jet experiment is achieved (first grating 700 lines/mm,  $50\mu\text{m}$  exit slit, 100 eV). The whole beamline operates under UHV conditions of  $< 10^{-10}\text{ mbar}$ . The individual segments of the beamline are separated by UHV valves, and several ion getter pumps provide the necessary pumping capacity. To avoid thermal damages, the first optical elements are water-cooled. A beam shutter closes the beamline and absorbs X-ray radiation that is created during the injection. Pressure gauges provide signals to a safety system (interlock) that controls the action of a number of valves in case of unexpected pressure changes. It also prevents opening of the valves unless the pre-set pressure limits are met. The photon flux can be measured by detecting the photoelectric current from a gold mesh or a photodiode placed directly after the exit slit.